Lab on a Chip

PAPER

View Article Online
View Journal

Cite this: DOI: 10.1039/d6lc00275g

Auto-SELEX: a fully automated microfluidic platform for rapid discovery of high-affinity aptamers

Yang Bu,[a] Yuze Liu,[b] Anni Hu,[b] Yung Ching Lee [a] and Levent Yobas *[ab]

Aptamers are synthetic single-stranded oligonucleotides that fold into defined three-dimensional structures, enabling high-affinity and highly selective target recognition, and are increasingly explored as alternatives to antibodies in diagnostics and therapeutics owing to advantages in production cost, reproducibility, thermal stability, and generation time. However, the conventional systematic evolution of ligands by exponential enrichment (SELEX)—an iterative *in vitro* selection process that screens large random nucleic-acid libraries for target-binding sequences—remains labor-intensive, time-consuming, and resource-demanding, often requiring specialized expertise while exhibiting poor efficiency and low success rates. Here, we present Auto-SELEX, a fully automated microfluidic platform that enables rapid discovery of ssDNA aptamers against protein targets, completing each selection round in approximately 30 min, as opposed to days or weeks typically required by conventional or competing approaches. Auto-SELEX integrates continuous-flow free-solution electrokinetic partitioning of target-bound aptamers across an artificial sieve without immobilization or iterative washing, together with plasmonic bead-based PCR using gold nanorods for rapid amplification and library regeneration with integrated purification and thermal elution. The platform enables rapid, automated, and effective aptamer discovery, substantially accelerating the SELEX workflow as demonstrated using two structurally and biochemically distinct protein targets, human immunoglobulin E (IgE, ~190 kDa) and vitronectin (~75 kDa), yielding high-affinity and target-specific DNA aptamers after only two to three selection rounds, with dissociation constants below 20 nM and 100 nM, respectively.

Received 1st April 2026,
Accepted 12th May 2026

DOI: 10.1039/d6lc00275g

rsc.li/loc

1 Introduction

Aptamers are synthetic short single-stranded DNA (ssDNA) or RNA (20–100 nucleotides) that bind diverse biological targets with high affinity and specificity.[1–3] Often termed chemical antibodies, they offer key advantages over monoclonal antibodies, including better thermal stability, lower cost, minimal batch-to-batch variation, and ease of labeling or conjugation without affinity loss. Aptamers are used in biosensors for detecting pathogens,[4,5] biomarkers,[6,7] and contaminants,[8,9] as well as in therapeutics for treating cancers,[10,11] infectious diseases,[12,13] and immune disorders.[14,15] Their utility is expanded through incorporating them into delivery systems such as aptamer–drug conjugates or functionalized nanomaterials.[16–18]

Aptamers for specific targets are generated through an iterative process known as systematic evolution of ligands by exponential enrichment (SELEX).[19–21] The process begins with a highly diverse library of randomized oligonucleotides (10^{14}–10^{16} sequences), which undergoes progressive enrichment for high-affinity binders over successive cycles. Each cycle consists of incubating the target with the library, partitioning target-bound sequences and then amplifying them *via* PCR or reverse transcriptase PCR (RT-PCR), to regenerate the library for subsequent cycle. Conventional SELEX is slow, laborious, and prone to variability. It typically requires many cycles over several weeks, consumes large amounts of targets and reagents, and offers limited control over selection stringency. Manual workflows introduce PCR bias, reduce library diversity, and make targeting complex molecules challenging. These limitations, coupled with laborious steps and poor scalability, highlight the need for an automated platform that enables precise control, minimize error, and accelerate aptamer discovery.

Microfluidics can meet this need by enabling precise fluid control at the microscale, reducing reagent consumption, and more importantly integrating multiple steps into a single

[a] *Department of Electronic and Computer Engineering, The Hong Kong University of Science and Technology, Clear Water Bay, Kowloon, Hong Kong SAR, China.*
E-mail: eelyobas@ust.hk; Fax: +852 2358 1485; Tel: +852 2358 7068
[b] *Department of Chemical and Biological Engineering, The Hong Kong University of Science and Technology, Clear Water Bay, Hong Kong, SAR, China*

automated platform. By miniaturizing the SELEX workflow, microfluidic systems accelerate selection cycles, improve stringency control, and minimize human intervention. Pioneering microfluidic studies primarily focused on aptamer partitioning, while relying on off-chip aptamer amplification and library regeneration. They used approaches such as bead-based separation[22,23] or sol–gel encapsulation.[24] However, immobilizing targets on beads can distort their native conformation and mask binding domains while sol–gel encapsulation faces mass-transfer constraints and non-specific binding. Meanwhile, capillary electrophoresis-SELEX (CE-SELEX)[25–27] performs partitioning in free solution and thus preserves the native conformation of the target while minimizing non-specific interactions. CE-SELEX enables rapid, high-resolution separation of bound and unbound species based on differential electrophoretic mobilities. A derivative of CE-SELEX, namely non-equilibrium CE of equilibrium mixtures (NECEEM), further allows real-time assessment of the bulk affinities of enriched libraries as well as individual sequences.[28,29] NECEEM adopts a non-SELEX strategy, identifying binders without the intermediate amplification and purification steps. However, these methods limit the library size due to the small sample injection volume. Additionally, fraction collection through a single outlet is challenging and must be carefully timed. These limitations are addressed in micro-free flow electrophoresis (μFFE), where continuous-flow operation removes sample volume constraints and directs separated fractions to distinct outlets.[30] The sample is continuously streamed into a flow chamber, separated under an orthogonal electric field, and collected in parallel.

Later studies, though limited in number, have increasingly integrated aptamer selection, amplification, and intermediate steps into single microfluidic platforms, moving toward automated SELEX. Hybarger *et al.* demonstrated a valve-controlled microfluidic system based on microline architecture for the selection of anti-lysozyme aptamers.[31] Lee and co-workers subsequently developed a series of integrated platforms with broader applicability. They first integrated magnetic bead-based partitioning with on-chip PCR to generate aptamers against C-reactive protein and alpha-fetoprotein, completing each round in 60 min.[32,33] They also extended this approach to the selection of aptamers against the influenza A/H1N1, with validation in clinical specimens such as throat swabs.[34] Subsequently, they demonstrated the simultaneous selection of aptamers against multiple cardiovascular biomarkers, completing five selection rounds in 8 h.[35] Kim *et al.* employed electrophoretic oligonucleotide manipulation to couple bead-based selection with PCR, identifying high-affinity aptamers in as few as three rounds.[36] Olsen *et al.* refined this concept with a hybrid electrokinetic–hydrodynamic transport scheme, selecting aptamers against immunoglobulin E (IgE) in four rounds over approximately 10 h.[37] Despite these advances, all reported platforms rely on immobilizing targets on beads to enable partitioning, which can perturb native target conformation and increase non-specific interactions. To date, a fully automated system that integrates selection, amplification, and library regeneration while eliminating target immobilization is still lacking.

Here, we introduce Auto-SELEX, a fully automated microfluidic platform that integrates continuous-flow electrokinetic partitioning of aptamers with plasmonic bead-based PCR amplification, thereby streamlining the entire SELEX workflow for a given protein target. Auto-SELEX comprises a control unit with a touchscreen interface and an operational unit that houses a disposable microfluidic cartridge in which the entire selection workflow is executed. The cartridge employs a multiscale architecture, where millimeter-scale vacuum-driven chambers enable transport of large fluid volumes through microfluidic channels and valves. Auto-SELEX leverages two key innovations previously developed in our laboratory: (i) continuous-flow electrokinetic separation of macromolecules using an artificial sieve formed by a two-dimensional (2D) capillary-well (CW) array,[38–40] and (ii) plasmonic bead-based PCR performed using gold nanorods (AuNRs) within a vacuum-driven chamber.[41,42] The overall Auto-SELEX workflow incorporating these elements is illustrated in Fig. 1. We first present experimental results from the aptamer selection and amplification modules, followed by a demonstration of fully autonomous aptamer discovery against two protein targets. Human immunoglobulin E (IgE, MW ~ 190 kDa) serves as a benchmark target with previously reported aptamers obtained using conventional SELEX[43] and CE-SELEX,[44] while vitronectin —a multifunctional glycoprotein distinct from IgE in molecular weight (~75 kDa), isoelectric point, and biological function— provides a contrasting target to further assess the generalizability of Auto-SELEX. Notably, vitronectin, despite its roles in cell adhesion and angiogenesis, remains underexplored in aptamer discovery. The entire Auto-SELEX workflow, including incubation, selection and amplification proceeds without manual intervention with each round completed in

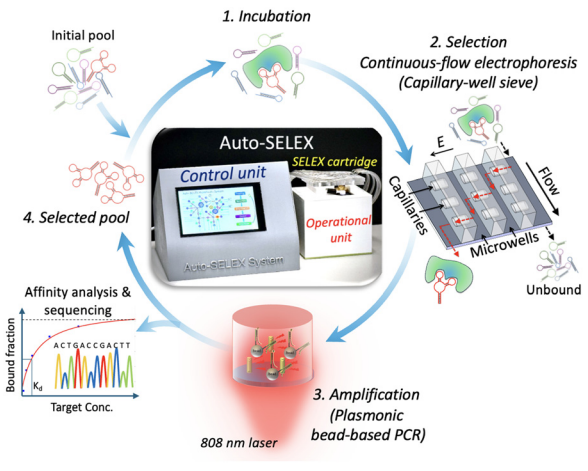

Fig. 1 Auto-SELEX workflow and key functional modules: continuous-flow electrokinetic selection of aptamers across an artificial sieve (two-dimensional capillary-well array) following target incubation, and plasmonic bead-based PCR amplification of selected aptamers within a vacuum-driven chamber to regenerate the library for subsequent cycles.

approximately 30 min. Within only two to three rounds, Auto-SELEX successfully isolates DNA aptamers against both IgE and vitronectin, achieving dissociation constants (K_d) below 20 nM and 100 nM, respectively.

2 Experimental

Reagents and materials

The FAM-labelled forward primer (5′-/6-FAM/CTA CCT ACG ATC TGA CTA GC-3′), biotin-labelled reverse primer (5′-biotin-GGA ACT ACA TGA GAG TAA GC-3′), and FAM-labelled randomized ssDNA library (5′-/6-FAM/CTA CCT ACG ATC TGA CTA GC-(40 random bases)-GCT TAC TCT CAT GTA GTT CC-3′) and the selected sequences were synthesized by Integrated DNA Technologies, Inc. (Coralville, IA). Human myeloma IgE protein was purchased from Sigma Aldrich (St. Louis, MO). IgG and IgM from human serum, as well as bovine serum albumin (BSA) were purchased from Sigma-Aldrich. Human vitronectin was purchased from Thermo Fisher Scientific (Waltham, MA). Streptavidin-coated 2.8 μm magnetic beads were obtained from Invitrogen (Carlsbad, CA). KOD One™ PCR Master Mix was sourced from TOYOBO (Osaka, Japan). PCR polymer-functionalized AuNRs (PCR-808-DIH-50-1) with 10 nm in diameter and 41 nm in length were obtained from Nanopartz (Loveland, CO). Nuclease-free water was supplied by Thermo Fisher Scientific (Waltham, MA). Bead functionalization buffer (10 mM Tris-HCl pH 7.5, 1 mM EDTA, 2 M NaCl) and 1× TGK buffer (125 mM Tris-HCl, 960 mM glycine, 25 mM KH_2PO_4; pH 8.3) were prepared using chemicals from Sigma-Aldrich and Avantor (Radnor, PA). Agarose, SYBR™ Safe DNA Gel Stain, and DNA loading buffer were procured from Invitrogen. PDMS base and curing agent (Sylgard 184) were purchased from Dow Corning (Midland, MI). PDMS membrane (~300 μm thick) was sourced from Westru (Hangzhou, China). SU-8 2050 negative photoresist was obtained from MicroChem (Westborough, MA). Pneumatic tubing and platinum electrodes were obtained from Cole-Parmer (Vernon Hills, IL) and Leego Precision Alloy (Shanghai, China), respectively.

System hardware

System hardware comprises components housed within custom 3D-printed enclosures of the control and operational units (Fig. S1). The control unit includes an Arduino GIGA R1 WiFi microcontroller board with display shield (Arduino, Ivrea, Italy) on a custom PCB, a high-voltage supply (WRB12200, NengDa Power Tech, Guangzhou, China) a miniature pump (CJWP08-AB03A10, Conjoin, Xiamen, China), an I^2C pressure sensor (MPX5700AP, NXP Semiconductors), and solenoid valves (LHDA0533115H, The LEE Company, Westbrook, CT). The operational unit incorporates a cartridge receptacle, an 808 nm laser module (Arm Laser, Shenzhen, China), a compact cooling fan (AFB0512MA, Delta Electronics, Taipei, Taiwan), a K-type thermocouple (Omega Engineering, Norwalk, CT), a permanent magnet (HuiLunTe Magnets, Jiangsu, China), and a micro servo with a motorized positioning arm (SG90, TowerPro, Taipei, Taiwan).

Selection chip

The sieve was fabricated on 4-inch silicon carrier wafers using a two-mask UV lithography process (Fig. S2). First, a 5 μm-thick low-temperature oxide (LTO) layer was deposited *via* chemical vapor deposition (CVD). This layer was patterned through advanced oxide etching (AOE) after the first lithography step, forming trenches 2 μm wide and deep. Subsequently, a 100 nm-thick low-stress silicon nitride (LSN) diffusion barrier and a 6 μm-thick phosphosilicate glass (PSG) structural layer were deposited by CVD, creating self-enclosed channels within the trenches. The PSG was annealed at 1000 °C for 30 min, turning the channels into tubular capillaries approximately 800 nm in diameter, which was further reduced *via* extended thermal annealing. Chemical mechanical polishing (CMP) was applied to achieve surface planarity before the second lithography step. The second mask defined reservoirs and microchannels (≈2 μm wide, 5 μm deep) *via* UV lithography and AOE, defining the capillary openings and wells. The remaining LTO layer in the wells served as electrical insulation. The completed chip was imaged using a scanning electron microscope (SU8600, Hitachi, Tokyo, Japan) and bonded to the cartridge backside by oxygen-plasma surface treatment (29.6 W, Harrick Plasma, 60 s).

Microfluidic cartridge

The cartridge was built using a multilayer soft lithography process. Three distinct masters were prepared by patterning 100 μm-thick SU-8 (SU-8 2050) layers on 4-inch silicon wafers *via* UV lithography. These masters were then used to cast the fluidic, pneumatic, and cap layers after overnight silanization with chlorotrimethylsilane. PDMS base and curing agent were mixed at a 10 : 1 ratio and then degassed in a desiccator to remove air bubbles. The mixture was cast onto the respective masters and cured on a hot plate at 120 °C for 20 min, after which the pneumatic and cap layers were peeled off, with thicknesses of approximately 5 mm and 7 mm, respectively. Pneumatic access ports (~1 mm diameter) were then punched using a biopsy needle. For the fluidic layer, the mixture was spin-coated onto its master at 500 rpm for 25 s and cured on a hot plate at 120 °C for 10 min, yielding a layer approximately 500 μm thick. Assembly began by bonding the pneumatic layer to a 300 μm-thick PDMS membrane after an oxygen-plasma surface treatment (Harrick Plasma, 30 W, 60 s), and the bond strength was reinforced on a hot plate at 120 °C for 10 min. This subassembly was punched to create inlet reservoirs and vacuum-driven chambers (~3 mm diameter), then aligned and bonded to the fluidic layer *via* a second surface treatment with oxygen plasma. Finally, the entire stack was aligned and bonded to the silicon selection chip after a third plasma surface treatment, and the cap layer was placed on top, completing the multilayer hierarchical cartridge. The chip was filled with 1× TGK buffer from cartridge reservoirs and incubated at 4 °C for over 48 h to condition electroosmotic flow.

Bead and sample preparation

A 50 μL aliquot of streptavidin-coated magnetic beads was washed and resuspended in 50 μL of functionalization buffer containing 2 μL of 100 μM biotinylated reverse primer. The suspension was incubated overnight to immobilize the primer onto the bead surface, after which the beads were washed to remove unbound reverse primers and resuspended in 50 μL of 1× TGK buffer. To prepare the sample for SELEX, the random ssDNA library was annealed at 90 °C and cooled to room temperature, followed by incubation with target protein in 1× TGK buffer for 20 min at room temperature.

Selection experiments

The sample containing either FAM-labeled ssDNA library alone or pre-incubated with target protein was first loaded into the main inlet of the selection chip. Sheath buffer (1× TGK) was loaded into the two side inlets. Pneumatic tubings were then inserted into the respective control ports to enable fluidic driving. To characterize the electrokinetic separation, the cartridge was subsequently placed on the stage of an epifluorescence microscope (Eclipse, Nikon, Tokyo, Japan) equipped with an electron-multiplying charge-coupled device (EMCCD) camera (iXon3897, Andor, Belfast, UK) for real-time visualization. A pair of platinum wires were immersed into corresponding sieve reservoirs (I4 and I5) and connected to a supply (uEP01-300, LabSmith Inc., Livermore, CA) with a tuneable output up to 300 V, for determining the required selection voltage. A vacuum of approximately 65 kPa was simultaneously applied to both sieve outlets (chambers C2 and C3), drawing a sample stream into the sieve. The stream exited the sieve through the primary outlet (chamber C2) in the absence of an applied voltage. With a steady voltage applied, by tuning the voltage, a threshold was identified above which a fraction of the binary mixture became sufficiently deflected to exit the sieve through the alternative outlet (chamber C3) while the remaining portion continued to exit through the default outlet (chamber C2). Images were acquired and fluorescence intensity profiles were analyzed using ImageJ software (NIH, Bethesda, MD).

Amplification experiments

Amplification was carried out with the cartridge mounted onto the operational unit with the pneumatic tubings inserted into respective ports connected to the control unit. A mixture containing 8 μL of 2× KOD One™ PCR Master Mix, 2 μM FAM-labeled forward primer and 3.36 nM AuNRs was transported from reservoir I6 to chamber C3, which contained a 1 μL template of 10 nM ssDNA library. The combined mixture was then drawn through mixer II into chamber C4. Subsequently, 7 μL reverse primer-functionalized magnetic beads (60 μg) was introduced from reservoir I7, yielding a final reaction volume of approximately 16 μL. This volume partially filled the PCR chamber, forming a liquid column capped by an air phase. The column was heated from below by an 808 nm laser irradiation (0.28 W mm^{-2}, spot diameter ~3 mm) to 92 °C for denaturation and then cooled under a directed airflow from a cooling fan to 47 °C for combined annealing/extension within each cycle. Temperature was monitored in real time using a K-type thermocouple immersed into the liquid column, and regulated *via* a PID feedback loop. Following amplification, the magnetic beads were transferred into an Eppendorf tube, washed three times with ultrapure water and then deposited onto a glass slide for fluorescence imaging. Bead fluorescence intensities were measured using ImageJ software (NIH, Bethesda, MD), with more than 50 individual beads analyzed for each condition. For thermal elution characterization, amplified beads were imaged after plasmonic heating for defined durations (3, 6, and 9 s) to evaluate the decrease in fluorescence signal.

Auto-SELEX experiments

Auto-SELEX workflow was initiated with the cartridge mounted onto the operational unit—with all reservoirs pre-filled as designated in Table S1, the PCR chamber aligned with the laser path, and the pneumatic tubings and platinum wire electrodes preinstalled within the cap layer connected to the control unit (Fig. S1B). The control unit, with the press of a button, executed a workflow, consisting of a programmed sequence of steps, each with optimized timing. These included switching the specified solenoid valves between atmosphere and vacuum (65–95 kPa) for fluid transport and valving; delivering high voltage to the electrodes for aptamer selection; alternatingly activating the laser and cooling fan for amplification; and positioning of the permanent magnet relative to the PCR chamber to hold or release the magnetic beads. The selection step lasted about 2 min, processing approximately 90 nL of the mixture through the 2D CW sieve under an applied voltage of 200 V. This corresponds to 2.7×10^9 target molecules and 5.4×10^{11} random sequences with a library-to-target ratio of 200. The amplification step required about 10 min to complete 25 thermal cycles (denaturation at 92 °C and annealing/extension at 47 °C). The purification step took approximately 2 min, during which the magnetic beads were washed three times with wash buffer (1× TGK) by sequentially filling and emptying the PCR chamber. Following purification, the PCR chamber was filled with 1× TGK buffer containing 1.68 nM AuNRs to enable plasmonic heating during the subsequent thermal release. Thermal release was then achieved by 6 s laser exposure. Prior to initiating the next SELEX round, the system performed a series of cleaning steps to prevent cross-contamination. The eluted ssDNA was then mixed with fresh target protein and incubated in chamber C1 for 15 min to allow complex formation. Each SELEX round required approximately 30 min of automated operation, except for the first round, which was shorter due to the absence of the on-board incubation step. Independent experiments were conducted using a fresh cartridge for each run, with each run terminated after 1, 2, or 3 rounds. The eluted samples collected from reservoir C6 underwent off-chip analysis.

Affinity and specificity

The dissociation constants (K_d) were measured using fluorescence polarization (FP) on a FlexStation® 3 Multi-Mode Microplate Reader (Molecular Devices, San Jose, CA). Briefly, 10 nM FAM-labeled aptamers, either from synthesis or off-chip amplified pools were titrated with increasing concentrations of target protein, with measurements conducted up to 200 nM for human IgE and 500 nM for human vitronectin. Parallel and perpendicular fluorescence intensities (λ_{ex} = 485 nm, λ_{em} = 528 nm) were recorded, and polarization values and bound fractions were calculated with corrections for intensity changes as previously described.[30] Specificity was assessed by measuring binding of the selected sequences to a panel of non-target proteins.

Next-generation sequencing (NGS)

NGS analysis of aptamer pools was performed by Sangon Biotech (Shanghai, China). Briefly, libraries were prepared using a two-step PCR protocol. The first PCR (25 μL) contained 2 μL DNA (10 ng μL^{-1}), 1 μL each of amplicon forward and reverse primers (10 μM), and 15 μL of 2× Kapa HiFi ReadyMix. Thermal cycling consisted of 98 °C for 5 min, followed by 8 cycles of 98 °C for 30 s, 60 °C for 30 s, and 72 °C for 30 s, with a final extension at 72 °C for 5 min. Amplicons were verified by 1% agarose gel electrophoresis (TBE, SYBR Green I), purified using AMPure XP beads (Beckman Coulter, Brea, CA), and subjected to a second PCR (30 μL) containing 2 μL DNA (10 ng μL^{-1}), 1 μL each of indexed universal P5 and P7 primers (10 μM), and 15 μL of 2× Kapa HiFi ReadyMix. Cycling conditions were 98 °C for 3 min followed by 5 cycles of 94 °C for 30 s, 55 °C for 20 s, and 72 °C for 30 s, with a final extension at 72 °C for 5 min. Amplicons were purified (AMPure XP), quantified, pooled and sequenced using paired-end 300 bp reads (PE300) on an Illumina NextSeq2000 platform (Illumina Inc., San Diego, CA).

Data analysis

Raw reads were processed by adaptor trimming with Cutadapt (v1.2.1), quality trimming ($Q < 20$) at the 3′ end using PRINSEQ-lite (v0.20.3) and *de novo* chimera removal using USEARCH (v11.0.667) with default parameters. Raw reads were further filtered using a custom Python script to retain only sequences exhibiting perfect matches to both primer regions. The resulting reads were then processed using FASTAptamer 2.0 for sequence counting and statistical analysis. Conserved sequence motifs were identified by analyzing sequences using MEME (Multiple EM for Motif Elicitation) Suite 5.9, with motif lengths constrained between 6 and 12 nucleotides. The identified motifs were then mapped back to the initially sequenced library using FIMO (Find Individual Motif Occurrences), a component of the MEME Suite,[45] to determine the occurrence frequency of each motif. The most abundant sequences were selected as candidates for synthesis and subsequent affinity characterization. Secondary structures and corresponding minimum free energies (ΔG) of candidate aptamers were predicted using the UNAFold (MFold) web server (http://www.unafold.org).[46]

3 Results

Auto-SELEX

Auto-SELEX comprises a control unit and an operational unit along with an accompanying microfluidic cartridge (Fig. S1). The control unit houses a microcontroller that coordinates the overall workflow, a mini-pump and an array of solenoid valves to actuate suction for vacuum-driven chambers and microvalves, a high-voltage power supply for the electrokinetic aptamer selection module, and a touchscreen user interface for system control. The operational unit accommodates the disposable microfluidic cartridge and incorporates an 808 nm laser source and an active cooling fan to enable plasmonic thermocycling and thermal elution. It also includes a permanent magnet mounted on a motorized positioning arm to immobilize magnetic beads during purification wash and elution steps.

Fig. 2A presents a photograph of the microfluidic cartridge together with a cross-sectional schematic illustrating its multilayer architecture. From top to bottom, the cartridge comprises: a cap layer, which provides pneumatic access microchannels to vacuum-driven chambers and microvalve cavities; a pneumatic layer, which defines the microvalve cavities, pneumatic microchannels and the vacuum-driven chambers; a membrane layer, which locally deflects under applied suction and enables pneumatic microvalve actuation; a fluidic layer, which routes liquids to and from the vacuum-driven chambers through microchannels, and a silicon chip, which performs electrokinetic separation using a 2D CW sieve array. All polymer layers are fabricated from polydimethylsiloxane (PDMS), with microchannels defined by micromolding, while reservoirs and chambers are formed by punching the respective layers before or after assembly and bonding.

As shown in Fig. 2B, the cartridge contains a set of reservoirs (I1–I11) for samples, reagents, buffers, and magnetic bead and AuNRs suspensions. Liquid handling and processing are carried out in vacuum-driven chambers (C1–C8) with capacities up to 30 μL, while pneumatically actuated, normally closed microvalves (V1–V13) provide precise fluidic control. The design further incorporates two micromixers: mixer I homogenizes the target protein and aptamer library beginning from the second selection round, and mixer II mixes the selected target–aptamer complexes with the PCR master mix containing forward primers and AuNRs prior to amplification. The design is further detailed through individual layer layouts and photographs acquired prior to assembly in Fig. S3.

Auto-SELEX leverages vacuum-driven chambers to facilitate liquid transport throughout the fluidic circuit. These millimeter-scale chambers, equipped with a top-access vacuum port and bottom-access microchannels for sample/reagent delivery and withdrawal, provide substantially larger capacity than microfluidic chambers. The applied vacuum

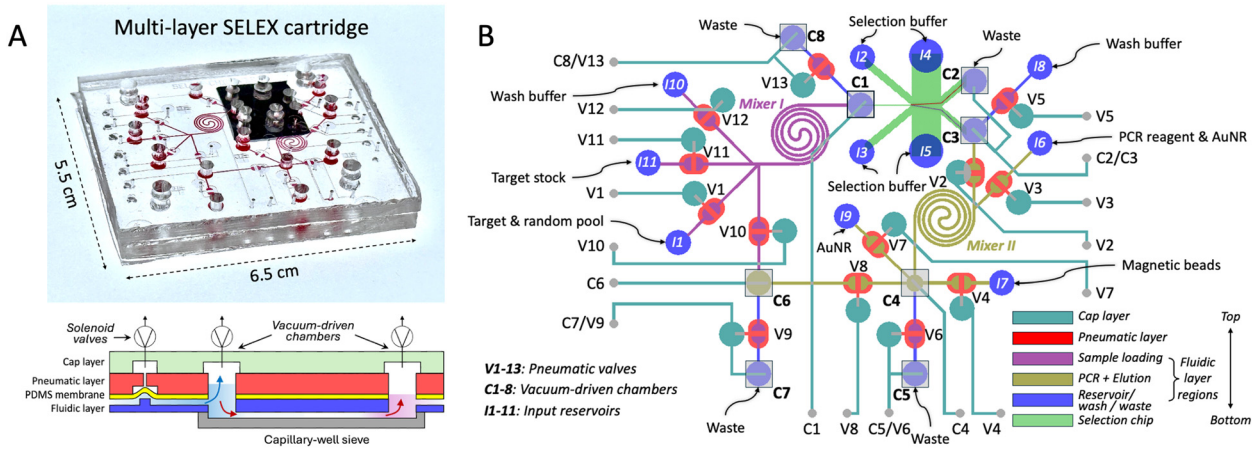

Fig. 2 (A) The microfluidic cartridge filled with red dye for visualization (top) and the corresponding cross-sectional schematic illustrating its multilayer architecture (bottom). (B) Composite fluidic layout of the cartridge, comprising (from top to bottom) the capping and pneumatic layers enabling vacuum delivery to valves and chambers, an elastomer membrane layer for valve actuation, a fluidic layer for sample and reagent routing and storage, and a silicon chip incorporating the artificial sieve for aptamer selection. Color denotes the layout within different structural layers and the fluidic layer functional regions.

level is deliberately limited so that each chamber is only partially filled, leaving an air buffer above the liquid to prevent unintended withdrawal. Liquid is transferred out of a chamber by venting it to atmosphere while applying vacuum to a downstream chamber, thereby drawing liquid from one chamber to the next. Precise and reproducible control of the transferred volume is accomplished by adjusting the vacuum application time, with cartridge-to-cartridge variation remaining below 10% based on measurements across fluidic paths in three independent cartridges (Fig. S4).

The workflow proceeds as follows. In the first cycle, a pre-incubated mixture of the target protein and randomized ssDNA library is transported from reservoir I1 to chamber C1 with valve V1 open. This mixture is then drawn into the 2D CW sieve by applying suction to chambers C2 and C3 simultaneously. Inside the sieve, the mixture stream is confined by sheath streams concurrently drawn from reservoirs I2 and I3. Under an orthogonal electric field applied *via* wire electrodes immersed in reservoirs I4 and I5, the sample stream bifurcates leading to predominant routing of unbound strands toward chamber C2 (waste) and target-bound strands toward chamber C3. Subsequently, the PCR master mix—containing forward primers and AuNRs—is first transported from reservoir I6 into chamber C3 *via* valves V2 and V3 (both open), where it mixes with the target-bound fraction. With valve V2 then kept open, the resulting mixture is delivered through mixer II into the PCR chamber (C4). Amplification begins once magnetic beads carrying reverse primers are transported from reservoir I7 into chamber C4 with valve V4 open. Thermocycling is achieved by alternating activation of the 808 nm laser source for plasmonic heating and the fan for active cooling. Post-PCR purification is performed with a permanent magnet positioned near the PCR chamber to retain the magnetic beads. The supernatant is removed by applying suction to waste chamber C5 with valve V6 open. Subsequently, wash buffer from reservoir I8 is drawn into chamber C3 with valve V5 open and into the PCR chamber with valve V2 open. After washing, the buffer is drawn to waste chamber C5 by opening valve V6. For the elution step, the permanent magnet remains in place as the elution buffer containing AuNRs is drawn from reservoir I9 into the PCR chamber through valve V7. A brief laser activation is then applied to induce thermal release of the bound product, after which the eluted product is transferred with valve V8 open into chamber C6 (product). The pool may then be directed into the next selection round or collected for downstream analysis.

Before initiating a subsequent cycle, cleaning steps are carried out by sequentially drawing wash buffer from reservoirs I8 and I10, with respective valves open into waste chambers C5, C7, and C8, thereby flushing the channels and chambers to prevent cross-contamination. Unlike the first selection cycle, each subsequent cycle begins by directing the regenerated library from chamber C6 into chamber C1 along with fresh target protein from reservoir I11 with valves V10 and V11 open; the two streams are co-flowed through mixer I and the resulting mixture is incubated within chamber C1 to allow complex formation before proceeding to the separation step. A detailed activation sequence of the workflow is provided in Fig. S5, and a complete visualization of the workflow is available in Movie S1.

Selection module

Aptamer selection takes place on a silicon chip featuring an artificial sieve mounted to the backside of the cartridge. The sieve comprises an anisotropic structure—a 2D CW array—in which capillaries intersect partitions separating parallel microchannels (wells). As described in Fig. 3A, the sieve is coupled to vacuum-driven chambers: one chamber near the

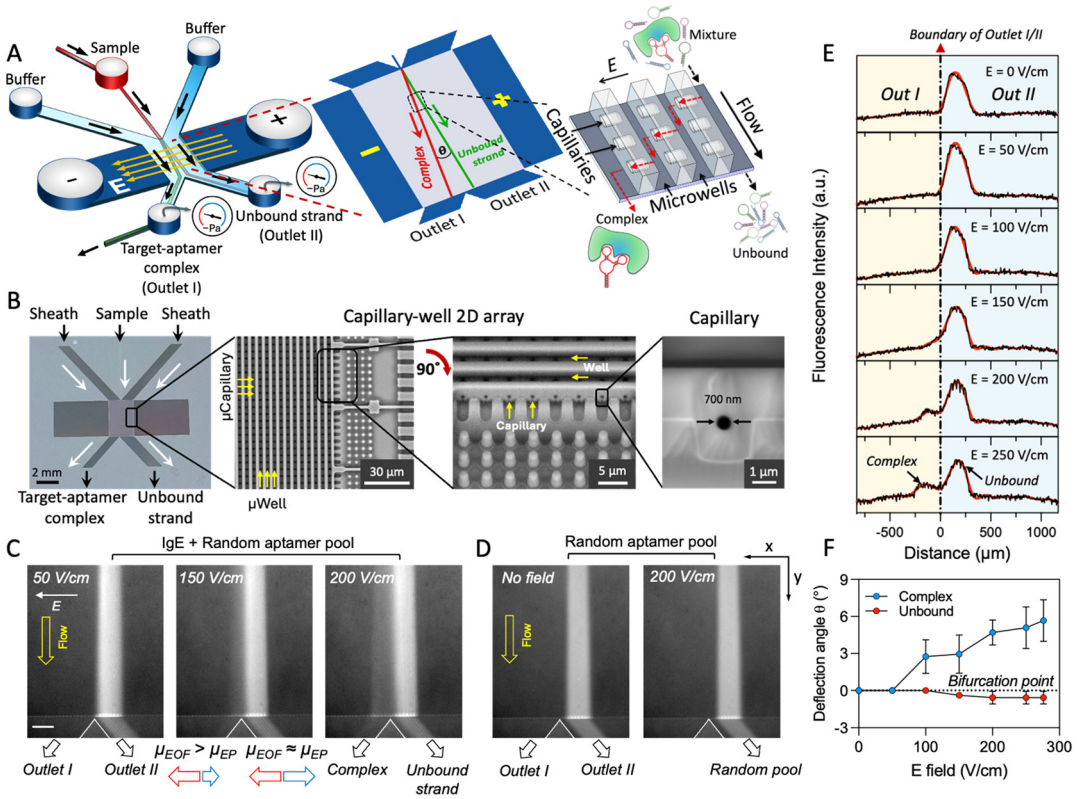

Fig. 3 Aptamer selection. (A) Schematic of continuous-flow electrokinetic separation of target-bound and unbound strands across the artificial sieve (2D CW array). The sample stream, flanked by sheath buffer, is drawn into the sieve by suction applied to two vacuum-driven chambers and bifurcates under a constant orthogonal electric field. (B) Photograph of the silicon chip incorporating the sieve, with scanning electron micrographs showing the sieve edge in both top and oblique views (rotated by 90° to reveal capillary openings), along with a close-up of an individual capillary opening. (C) Fluorescence images of a sample stream containing IgE and FAM-labelled randomized ssDNA library exiting the sieve under average electric fields of 50, 150, and 200 V cm^{-1}. At 50 V cm^{-1}, the stream exits through outlet II; at 150 and 200 V cm^{-1}, it bifurcates between outlets I and II. Increased field strength enhances deflection of the IgE–aptamer complex due to EOF overcoming opposing EP, while unbound strands exhibit minimal deflection owing to strong EP. Scale bar: 200 μm. (D) Fluorescence images of a sample stream containing only FAM-labelled randomized ssDNA library exiting the sieve with and without an average field of 200 V cm^{-1}. (E) Fluorescence intensity profiles at the sieve exit along the field direction, showing their evolution with increasing electric field strength. (F) Deflection angles of the IgE–aptamer complex and unbound strands as a function of average electric field strength. Error bars represent standard deviations based on measurements from three independent sieves.

inlet for incubating a mixture of target and randomized ssDNA library (sample) and a pair of chambers near the outlet for collecting the separated target-bound (complex) and unbound strands. Two additional reservoirs supply sheath streams that flank the sample stream, while another pair of reservoirs containing running buffer (1× TGK) and external wire electrodes delivers an orthogonal electric field to the streams *via* auxiliary microchannels. The use of the external electrodes that access the sieve through long auxiliary channels isolates the sieve from disrupting electrolysis byproducts.[30,40] During operation, suction applied to the outlet chambers draws a sample stream along with sheath streams into the sieve pre-filled with running buffer. As the mixture flows downstream, molecules translocate through the capillaries and migrate either along or against the applied electric field depending on their electrophoretic (EP) mobility and electroosmotic flow (EOF). As a result, the binary mixture is partitioned into two spatially distinct streams, each deflected at a characteristic angle, enabling continuous separation of target-bound complexes from unbound strands. This continuous-flow free-solution electrokinetic partitioning of target-bound strands replaces the bind–wash–elute steps required in conventional SELEX, with separation achieved through spatial resolution within the sieve.

Fig. 3B shows a planar view of the silicon chip with inset images highlighting uniform capillary openings. The separation region consists of a periodic 2D CW sieve array measuring 3.5 mm × 2.2 mm, comprising capillaries 2 μm in length and 700 nm in diameter, intersection microchannels 2 μm wide and 5 μm deep (pitch: 4 μm). These capillaries are self-enclosed channels formed by depositing a doped glass layer into trenches patterned by standard UV lithography. Subsequent thermal reflow reshapes the channels into tubular profiles, followed by further thermal annealing to gradually reduce the capillary diameter—eliminating the need for advanced nanolithography (Fig. S2). Unlike slit-based designs that impose 1D confinement, these capillaries provide 2D confinement, generating larger

entropic barriers at their entrances that enable high-voltage operation with improved separation resolution.[38,39]

In Fig. 3C and Movie S2, fluorescence images present sample streams—each containing a mixture of FAM-labeled randomized ssDNA strands and target IgE incubated for 15 min—as they traverse the sieve under varying electric field strengths. At a low field strength of 50 V cm^{-1}, no discernible separation occurs; the stream exhibits negligible deflection, flowing into the default outlet (outlet II), a consequence of the lateral offset between inlet and outlet in the device design (see the layout in Fig. S2). Increasing the field strength to 150 V cm^{-1} produces a faint secondary stream deflected toward the alternative outlet (outlet I), while the primary stream continues through outlet II. At 200 V cm^{-1}, the secondary stream shows greater deflection with the primary stream remaining largely unaffected. The low fluorescence intensity of the deflected stream suggests its association with complexes as the random library offers only a small fraction of aptamers specific to the target protein. This is further supported by the absence of the secondary stream when the sample contains only FAM-labeled random library despite under 200 V cm^{-1} (Fig. 3D). Based on these images, the field-dependent evolution of intensity profiles at the sieve exit along the field is depicted in Fig. 3E. The fluorescence intensity of the primary peak is reduced as the secondary peak emerges with the increased field strength. However, the secondary stream spreading prevents the two peaks from being fully resolved. This can be due to the parabolic velocity profile of hydrodynamic flow, which creates a distribution of residence times and thus a range of lateral migration distances as molecules pass through the sieve, spending different amounts of time under the electric field. Similarly, separation of target-bound ssDNA complexes from the unbound ssDNA library through the sieve is also observed for human vitronectin (~75 kDa), despite the smaller size of the target protein (Fig. S6).

Separation is governed by EOF counteracting EP across the sieve, which mainly causes target-bound complexes to deflect due to their weaker EP mobility in relation to unbound strands. Previous studies, including CE-SELEX[44,47,48] and μFFE-SELEX,[30,49] have shown that aptamer–IgE complexes exhibit minimal electromigration at near-neutral buffer (pH ~ 8.0; here pH 8.3) and with EOF suppressed, necessitating pressure rinses for visualization or collection of these complexes. This limited EP mobility is expected given the large size of IgE (~190 kDa) and its near-neutral net charge at a buffer pH close to its isoelectric point (pI ~ 9).[50] This also explains our choice of sample injection by pressure-driven flow instead of EP injection, which we utilized in our previous work regarding the use of the sieve for DNA separation.[40] While effective for DNA strands, EP injection is inadequate for introducing complexes into the sieve.

EOF dominates and deflects complexes toward outlet I whereas unbound strands with their strong EP mobility remain largely undeflected or slightly deflected in the opposite direction (Fig. 3F). Complexes and unbound strands accumulate in their respective chambers over time (Fig. S7). When EOF becomes excessive, it can override EP and deflect unbound strands as well, leading to separation failure—a condition observed when the sieve is used immediately after fabrication without prior incubation in running buffer (Fig. S8). Buffer incubation equilibrates the sieve surface by adsorbing counterions and stabilizing the electric double layer, thereby reducing EOF to the desired level for effective separation.[51]

Amplification module

Aptamer amplification is performed using bead-based PCR within a millimeter-scale vacuum-driven chamber, which offers greater capacity than typical microfluidic chambers while mitigating the issue of heat-induced bubbles. Bead-based PCR enables efficient strand separation of amplified aptamers through denaturation, allowing their elution following a purification wash. A key advantage of this solid-phase approach is the high recovery and purity of the enriched aptamers as compared to methods like asymmetric PCR[52] or exonuclease digestion.[53]

Bead-based PCR is schematically described in Fig. 4A. Laser-induced plasmonic thermocycling begins with annealing aptamer templates to reverse primers immobilized on streptavidin-coated magnetic beads through their biotinylated 5′ ends. In the initial cycle, these primers are extended to synthesize complementary strands. In subsequent cycles, the templates dissociate from the synthesized strands, leaving them to anneal with forward primers, while proceeding to re-anneal to new reverse primers for extension. The reverse primers hold dsDNA amplicons tethered on the beads while exponentially accumulating. Post-PCR strand separation of amplified templates for elution can be simply achieved through thermal denaturation under laser-induced plasmonic heating after purification wash. Throughout the process, a permanent magnet positioned adjacent to the chamber secures the beads in place.

Thermocycling is enabled by AuNRs dispersed in the reaction mixture. AuNRs convert irradiation into heat *via* localized surface plasmon resonance, resulting in volumetric and spatially uniform heating. Unlike thin-film heaters, this volumetric approach avoids thermal lag associated with substrate conduction, thereby enabling rapid heating of the millimeter-scale chamber content despite its relatively large thermal mass. Once laser irradiation ceases, active cooling is achieved through forced convection. Such rapid thermocycling, together with high-volume regeneration of enriched ssDNA libraries, is critical for minimizing the SELEX cycle time.

We previously characterized the amplification module as a standalone unit for ssDNA generation.[41] Building on this foundation, we further investigate here key parameters following its integration into cartridge. Fig. 4B presents the thermocycling performance for 16 μL PCR mixture with 60 μg magnetic beads and 1.68 nM AuNRs within a 3 mm-diameter chamber. The plots display temperature profiles for a 25-cycle run and a close-up of a representative cycle, showing

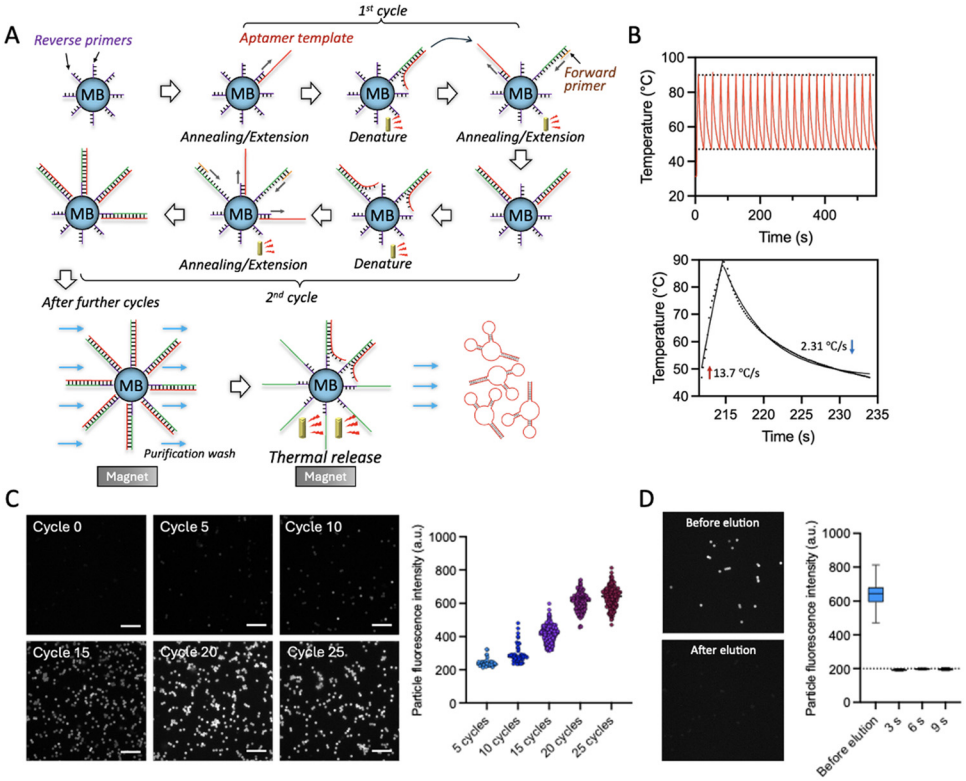

Fig. 4 Aptamer amplification. (A) Schematic describing the first and second cycles of bead-based PCR, followed by purification wash and thermal elution of amplified aptamers. (B) Thermal cycling performance of the vacuum-driven chamber: the temperature profile over 25 cycles and a representative single cycle with the exponential fittings. The chamber contains a 16 μL PCR mixture with 60 μg magnetic beads and 1.68 nM AuNRs. (C and D) Fluorescence microscopy images (50×) of beads and the corresponding fluorescence intensity plots: (C) before PCR and after purification wash at different PCR termination cycles, and (D) before and after thermal release using 3, 6, and 9 s laser exposures in 1× TGK elution buffer containing 1.68 nM AuNRs. Error bars indicate standard deviations based on measurements of more than 50 beads.

heating and cooling between 47 °C (annealing/extension) and 92 °C (denaturation). Under these conditions, 25 cycles are completed in under 10 min with average heating and cooling rates of 13.7 °C s^{-1} and 2.31 °C s^{-1}, respectively. This cycling duration is highly reproducible, with three independent cartridges completing 25 cycles in 9.3 ± 0.3 min (mean ± s.d.) The representative cycle exhibits characteristic exponential temperature rise and decay, with time constants of 1.67 s for heating and 5.27 s for cooling. Increasing AuNR concentration or reducing the chamber diameter can further accelerate thermocycling. However, these adjustments introduce errors in reaching target temperatures (Fig. S9).

The integrated module must reliably amplify aptamers delivered by the selection module to ensure the success of SELEX workflow. This functionality is verified using elution from the selection module (outlet I) as input, followed by post-PCR fluorescence imaging of beads before thermal release. Bead fluorescence is expected to rise with the number of thermal cycles as dsDNA amplicons accumulate on the beads, given the fact that both the forward primers and the ssDNA templates are FAM-labeled. Representative images along with the corresponding fluorescence intensity plot are shown in Fig. 4C. Significant increase in fluorescence occurs at the 15th thermal cycle and becomes more pronounced by the 20th cycle. Extra five cycles produce no significant increase in fluorescence, implying saturation, likely due to extension of all reverse primers. Consequently, reverse primers are consumed, necessitating a fresh bead supply for each SELEX cycle.

Thermal elution is preferred over alkaline wash as alkaline conditions could disrupt biotin–streptavidin bond and lead to unintended release of dsDNA.[54] However, prolonged heating may compromise streptavidin stability, despite its inherent thermal robustness; therefore, the heating period should be kept minimum. Fig. 4D reveals that a 3 s laser heating reduces fluorescence to background levels, indicating effective elution. During the Auto-SELEX workflow, a 6 s laser exposure is employed to ensure reliable elution while minimizing solvent evaporation. This elution step follows a purification wash, which removes residual reagents while magnetic beads bearing surface-tethered dsDNA amplicons are immobilized within the chamber using an external magnet. The brief laser-induced heating denatures the duplexes, selectively releasing the non-biotinylated ssDNA strands into solution while retaining the complementary strands on the beads *via* the biotin–streptavidin linkage. The released ssDNA is subsequently transferred downstream for collection and analysis or for use in the next selection round,

whereas fresh beads functionalized with reverse primers are introduced for subsequent amplification cycles. This on-chip thermal regeneration strategy avoids alkaline treatments that may compromise streptavidin integrity and enables rapid, high-purity ssDNA recovery.[41]

Automated SELEX

We performed independent Auto-SELEX runs terminated after one, two, and three rounds of selection and measured the affinities of the corresponding enriched pools against the targets [IgE, Fig. 5A(i); vitronectin, Fig. 5B(i)]. It should be noted that all datasets generated after one, two, or three selection rounds originate from independent Auto-SELEX runs, each using a fresh cartridge.

For both targets, the independently isolated pools show a consistent increase in binding affinity when comparing one-, two-, and three-round selections. However, these increases are modest compared to the affinity achieved in the single-round selection: the pool affinity improves by approximately seven-fold relative to the starting library, which exhibits no measurable affinity even at the highest target concentration tested for IgE (K_d > 200 nM), reaching a K_d value of 29.81 ± 7.44 nM [Fig. 5A(ii)] and by nearly five-fold relative to the starting library for vitronectin (K_d > 500 nM), with a K_d value of 128.1 ± 22.3 nM [Fig. 5B(ii)]. Such a pronounced improvement with only a single-round selection has been reported also for methods such as CE-SELEX,[47] MonoLEX,[55] and M-SELEX[56] yet contrasts with conventional SELEX, where early cycles are often limited by incomplete partitioning rather than true affinity discrimination. In those methods, rapid enrichment has been attributed to the use of a large molar excess of library over target (>10^4), which imposes strong selection stringency. In contrast, the library-to-target ratio used here is around 200—well within the range (10 to 1000) used in conventional SELEX.[57,58] Thus, the strong affinity gains observed for both targets after a single round reflect the efficient electrokinetic partitioning of target-bound complexes from weak binders and unbound sequences enabled by the artificial 2D CW sieve. Weakly bound or nonspecific sequences dissociate during repeated capillary translocations while being continuously advected downstream, whereas stable target-bound complexes remain intact, undergo translocation events that accumulate a net electrokinetic deflection. By decoupling affinity selection from surface interactions that promote non-specific binding and from washing steps that introduce inefficiencies, Auto-SELEX enables identification of strong binders in the first selection cycle rather than relying on cumulative amplification over many rounds. By contrast, conventional SELEX, limited by inefficient early-round partitioning compounded with PCR bias, necessitates repeated selection cycles to progressively enrich true binders, often obscuring affinity discrimination until late-stage convergence.

High-throughput sequencing reveals that the initial random library retains high integrity. After primer trimming, 99.72% of sequences fall within the expected 38–42 nt length range (Table S2). This length distribution is largely preserved in both the two- and three-round selection pools for both targets with a modest reduction observed in the two-round IgE pool, where ~98% of sequences fall within the expected range. A minor population of shorter sequences (<38 nt) persists at low

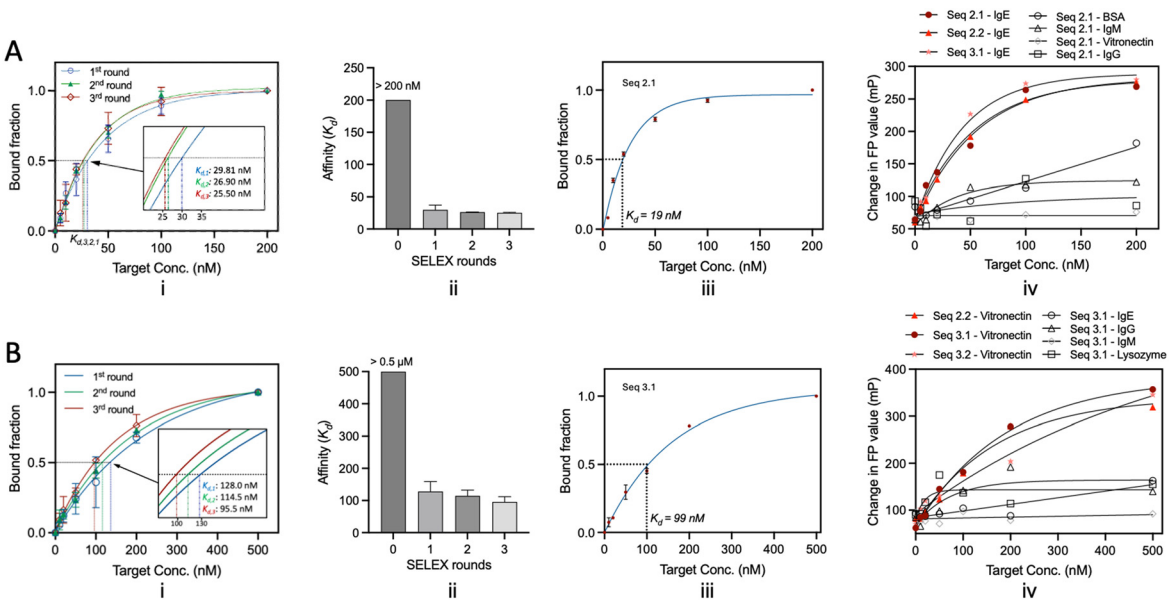

Fig. 5 Auto-SELEX evaluation. Affinity and specificity of aptamers against (A) human IgE and (B) human vitronectin assessed through FP. (i) Binding curves for ssDNA pools collected after one, two, and three rounds from independent Auto-SELEX runs. (ii) K_d values for the initial library and enriched pools. Error bars in (i) and (ii) indicate the standard deviation of affinity measurements obtained from three independent cartridges. (iii) Binding curve of the dominant sequence isolated after three rounds of Auto-SELEX (n = 3). (iv) Specificity assessment of the dominant aptamers in the enriched pools for cognate targets *versus* non-target proteins, each tested at 10 nM.

abundance (<2%), indicating minimal undesired byproduct formation. Sequence analysis further reveals that three-round selection pools contain a higher proportion of duplicate sequences than two-round selection pools. This effect is more pronounced for IgE than for vitronectin. Notably, the two-round IgE selection already exhibits a markedly higher fraction of duplicate sequences compared with the initial library, whereas the corresponding increase for vitronectin is marginal. These observations suggest more effective enrichment in the IgE-selected pools, which may explain their stronger apparent affinities. In contrast, the smaller size of vitronectin (75 kDa *vs.* 190 kDa for IgE) likely limits epitope availability and reduces the mass difference between free and target-bound aptamers, resulting in a less pronounced mobility shift, diminished discrimination between bound and unbound species, and consequently weaker enrichment.

The binding affinities of dominant sequences are summarized in Table 1. Their primary sequences and relative abundances in the corresponding pools, expressed as reads per million (RPM), are provided in Table S3. Sequences are labeled such that the first digit indicates the selection depth, and the second digit indicates the abundance rank within the respective pool. Dominant sequences between the two-round and three-round selections overlap, despite being independently conducted. For IgE, sequences 2.1, 2.2, 2.3, and 2.4 are identically recovered as sequences 3.1, 3.2, 3.4, and 3.3, respectively, while 3.5 overlaps with the lower-ranked sequence 2.83. A similar correspondence is observed for vitronectin with sequence pairs 2.1/3.1, 2.2/3.3, 2.3/3.2, and 2.6/3.4. These IgE and vitronectin aptamers exhibit dissociation constants within narrow ranges that encompass the corresponding bulk pool affinities: 19.0–28.2 nM and 98.5–157 nM, respectively.

Among the sequences tested, the most abundant aptamers, IgE and vitronectin sequences 2.1/3.1 exhibit the strongest binding affinities, with K_d values of 19.0 ± 1.95 and 98.5 ± 5.5 nM and the representative binding curves presented in Fig. 5A(iii) and B(iii), respectively. Both sequences display similar predicted secondary structures (Fig. S10 and S11), characterized by two hairpin stems extending in diverging directions and similar moderate Gibbs free energies of folding (ΔG = −3.57 *versus* −3.64 kcal mol^{-1}), suggesting a comparable degree of pre-folded conformation that may facilitate efficient target recognition without excessive structural rigidity.[59] In the IgE aptamer, conserved sequence motifs partially or entirely span both hairpins, whereas in the vitronectin aptamer motif coverage is limited to a single hairpin.

For IgE, sequence 3.5 also presents binding affinity (19.9 ± 1.8 nM) comparable to that of sequence 2.1/3.1, despite substantial differences in its primary sequence. Their predicted secondary structures show similarity (Fig. S10). In contrast, sequence 2.3/3.4, a close variant of 2.1/3.1 differing by only a few bases, exhibits a discernible reduction in binding affinity (19.0 *vs.* 25.3 nM) and a distinct predicted folding topology presenting only a single hairpin containing an internal loop. Notably, conserved sequence motifs are mainly located within single-stranded regions flanking the hairpin stem. This pronounced sensitivity of binding affinity to minimal sequence variation is consistent with prior SELEX studies,[60] which report that target binding can be markedly altered by even single-base substitutions, particularly near loop or junction regions. For vitronectin, the remaining aptamers predominantly adopt a single-hairpin architecture (Fig. S11) and exhibit weaker binding affinities.

Conserved sequence motifs are identified for both targets after three-round selection (Table S4). For IgE aptamers, three motifs are observed: AGCTAGTCAGTG (motif 1), ATCATGAAA TAT (motif 2), and AGATTMRTACAA (motif 3; M = A/C, R = A/G). For vitronectin aptamers, two motifs are identified: CCATSCTGWRGR (motif 1; S = G/C, W = A/T, R = A/G) and AACA TCATKAAA (motif 2; K = G/T). Comparison between selection depths shows higher relative motif-associated read abundance in the three-round selection than in the two-round selections, with fold differences of 4.2–5.6 for IgE and only ~1.3 for vitronectin (Table S4). These differences parallel the higher proportion of duplicate sequences observed in the three-round selections relative to the two-round selection, with a more pronounced increase for IgE than for vitronectin. Sequence logo analysis reveals highly similar motif architectures in the two-round and three-round selections, with increased information content and reduced positional degeneracy in the three-round pools (Fig. S12). Consistent with these observations, motif *E*-values are substantially lower at three rounds, indicating stronger statistical definition of the same motifs.

Apart from the most abundant aptamers (2.1/3.1), the other sequences listed in Table S3 do not bear any of the identified motifs except for IgE sequence 2.3/3.4, which carries close variants of motifs 1 and 2 at or near its termini, similar to IgE sequence 2.1/3.1. The two sequences also share a short motif, TACAAACATCAT (underlined in Table S3), which is identified by the MEME Suite only in the two-round selection, but not in the three-round selection. High-affinity binding is not strictly dependent on motif presence, as IgE sequence 3.5, which lacks any of the identified motifs, exhibits comparably high binding affinity to that of the motif-bearing IgE sequence 2.1/3.1.

Specificity validation demonstrates that the selected aptamers bind their intended targets with high affinity while showing minimal binding to non-target proteins tested [-Fig. 5A(iv) and B(iv)]. For IgE aptamers, the non-targets

Table 1 Dissociation constants (K_d) of IgE and vitronectin aptamers

Target	Aptamer	K_d (nM)
IgE	2.1/3.1	19.0 ± 1.95
	2.2/3.2	25.3 ± 0.70
	2.3/3.4	25.3 ± 2.50
	2.4/3.3	28.2 ± 0.80
	2.83/3.5	19.9 ± 1.80
Vitronectin	2.1/3.1	98.5 ± 5.50
	2.2/3.3	108 ± 2.60
	2.3/3.2	118 ± 9.50
	2.6/3.4	157 ± 13

include human IgG, IgM, vitronectin, and BSA. For vitronectin aptamers, non-targets include human IgE, IgG, IgM, and lysozyme. The low-level residual signals observed for certain non-targets likely reflect partial cross-interactions rather than strong nonspecific binding. For these off-targets, specificity can be further improved by introducing negative selection steps.

Both IgE- and vitronectin-selected pools retain substantial sequence diversity. The most abundant IgE aptamer, sequence 2.1/3.1, accounts for below 0.05% of total reads in the three-round selection, consistent with prior CE-SELEX studies in which dominant clones rarely exceed 1% even after multiple selection cycles.[27] This retention of sequence diversity is characteristic of free-solution electrokinetic partitioning, which efficiently separates binders from non-binders while limiting collapse of library complexity. To the best of our knowledge, none of the aptamer sequences identified here match those previously reported against IgE or vitronectin.[30,34,47,58] Importantly, none of the identified conserved motifs in the IgE or vitronectin aptamers coincide with those reported previously, consistent with the notion that variations in selection conditions can yield distinct sequence families. The binding affinities achieved here compare favorably with prior reports for both targets. For IgE, reported DNA aptamers span a wide range of dissociation constants (K_d = 1–84 nM) across diverse SELEX platforms, placing the 19.0 nM aptamer identified in this study well within the high-affinity range. For vitronectin, only a single aptamer has been described to date with a reported K_d value of 405 nM, highlighting the improved binding performance observed here (98.5 nM) for this small target.

4 Discussion

A comprehensive performance comparison between Auto-SELEX and the existing automated SELEX platforms is provided in Table S5. Across key metrics including processing time, automation level, and selection efficiency, Auto-SELEX demonstrates clear benefits: it completes each round in ~30 min, compared with 60–240 min for reported alternatives; it operates fully autonomously from sample loading to aptamer recovery, without manual intervention; and it achieves high-affinity aptamers in only 2–3 selection rounds, whereas most automated platforms require 4–10 selection rounds. These benefits arise from highly integrated workflow incorporating two key features: (i) continuous-flow electrokinetic partitioning in free solution across the 2D CW sieve, eliminating the need for target immobilization and iterative washing steps; and (ii) rapid plasmonic bead-based PCR leveraging AuNRs within vacuum-driven chambers with integrated purification and elution.

Auto-SELEX is best suited for specific targets that induce a clear electrophoretic mobility shift upon aptamer binding. For smaller targets, the relative changes in mass and charge are reduced, often resulting in only partial separation of bound and unbound species. Nevertheless, CE-SELEX has yielded aptamers for small molecules such as *N*-methyl mesoporphyrin (580 Da) by collecting the leading edge of a partially resolved peak.[61] Extending Auto-SELEX to smaller targets is therefore feasible, although it may require optimization of the collection band and, in some cases, an increased number of selection rounds. Future improvements, such as reducing the capillary diameter in the 2D CW sieve, may further enhance separation resolution and extend the applicability of Auto-SELEX to more challenging targets.

In terms of throughput, Auto-SELEX processes 90 nL of sample through the 2D CW sieve within a two-min selection window, corresponding to 2.7×10^9 target molecules and 5.4×10^{11} random sequences at a library-to-target ratio of 200. While this amount is larger than that typically handled in CE-SELEX, it remains much lower than in conventional SELEX. Owing to the continuous-flow operation, extending the selection window to tens of minutes would screen an order of magnitude more sequences without considerably prolonging the overall operation time. Further throughput gains could be realized by operating multiple cartridges in parallel. Even without such scaling, free-solution electrokinetic partitioning already enables strong affinity discrimination within a single cycle, whereas conventional SELEX relies on repeated rounds to gradually compensate for inefficiencies arising from nonspecific adsorption and surface-based washing.

Auto-SELEX operates reliably across consecutive selection rounds without any channel clogging given relatively large channel dimensions employed (100 μm deep and 300 μm wide). To prevent cross-contamination between selection rounds, extended vacuum-driven cleaning steps were introduced, ensuring thorough drying of the channels prior to liquid introduction in subsequent rounds. This optimization effectively mitigated occasional air bubble formation observed during early protocol development, which was attributed to residual liquid in the channels. Following implementation of this procedure, bubble formation has not been observed during routine operation. The sieve exhibited no detectable degradation in performance, indicating stable and repeatable operation over multiple selection rounds. This behavior is consistent with the expected short-term aqueous stability of the annealed PSG layer. As reported for phosphorus-doped oxide films, high-temperature annealing densifies the glass network and markedly suppresses moisture uptake relative to as-deposited films, resulting in improved chemical and mechanical stability.[62]

From a practical standpoint, operating Auto-SELEX requires only basic hands-on skills. The total hands-on time per run is below 2 min and the manual steps are limited to: (i) pipetting buffers and reagents into the designated cartridge reservoirs, and (ii) mounting the cartridge onto the operational unit and connecting the pneumatic tubings and wire electrodes. Once the cartridge is installed, the workflow is initiated by pressing the start button on the touchscreen interface. All subsequent operations—including fluid transport, electrokinetic separation, plasmonic PCR, bead washing, thermal elution, and inter-round cleaning steps—

are executed autonomously without further user intervention according to a pre-programmed control sequence.

The Auto-SELEX prototype and its disposable cartridge can be built at an estimated cost of $1500 and $30, respectively, in single-unit production. A detailed cost breakdown is provided in the bill of materials (Table S6). The system cost mainly arises from the use of over a dozen of solenoid valves; however, full automation can be achieved with as few as six solenoid valves if a pneumatic demultiplexer is integrated into the cartridge.[63] This approach would substantially reduce not only the overall cost but also the size and power consumption. While the cartridge cost estimate is currently based on a subsidized rate of an in-house cleanroom for low-volume fabrication, we anticipate comparable costs are achievable in manufacturing through further minimization of silicon real estate and economies of scale. Notably, the sieve is fabricated using standard silicon micromachining processes that are commonly available in commercial foundries, with capillary submicrometer critical dimensions realized through thermal reflow of a doped glass layer rather than advanced low-throughput nanolithography. Once calibrated, the thermal reflow process, yields highly uniform capillaries across wafers with batch-to-batch reproducibility.[39,64]

Manufacturing yield is expected to be primarily determined by layer-to-layer alignment during cartridge assembly and interlayer bonding strength. Our current yield exceeds 90%, based on more than 20 cartridges fabricated without the aid of dedicated alignment tools, owing to the high tolerance afforded by large features (3 mm chambers and valve seats wider than 500 μm). In manufacturing settings, yield is expected to improve further using vision-assisted pick-and-place alignment tools, often employed in semiconductor and chip packaging.

Conclusions

We have introduced Auto-SELEX, a fully automated microfluidic platform that executes the entire SELEX workflow within a single compact cartridge. Using two structurally and functionally distinct targets—human IgE (~190 kDa) and vitronectin (~75 kDa)—we have demonstrated that Auto-SELEX can autonomously generate high-affinity high-specificity DNA aptamers within only two to three selection rounds, achieving dissociation constants below 20 nM and 100 nM, respectively. Each selection round is completed in approximately 30 min, with hands-on time (below 2 min) primarily limited to cartridge loading and mounting. This per-cycle processing time is substantially shorter than that of conventional SELEX workflows, which require more than 2 weeks, as well as the limited number of existing automated microfluidic SELEX platforms that require 4–10 h to complete 2–4 selection cycles.[65–67]

Future work may extend Auto-SELEX to the aptamer selection against even smaller targets with subtler mobility differences, which are inherently more challenging to resolve but can be addressed by enhancing resolution through reduced sieve capillary diameters. In addition, Auto-SELEX provides a versatile platform for systematically investigating key stringency parameters—including target concentration, incubation time and temperature, and selection voltage—to further refine selection pressure and enable the discovery of aptamers with even higher affinity.

Author contributions

Conceptualization, L. Y., Y. B. Methodology, L. Y., Y. B., Y. L., A. H., and Y. C. L. Validation, Y. B., Y. L., A. H. Formal analysis, Y. B. Writing – original draft, review & editing, L. Y. and Y. B. Supervision, resources, project administration and funding acquisition, L. Y.

Conflicts of interest

L. Y. and Y. B. declare that they are inventors on a patent application related to the technology described in this work.

Data availability

The data supporting this article have been included as part of the supplementary information (SI).

Supplementary information: SI figures, tables and movies. See DOI: https://doi.org/10.1039/d6lc00275g.

Acknowledgements

This project was financially supported by the Innovation and Technology Support Programme (ITSP) of the Hong Kong Innovation and Technology Fund (Project No. ITS/048/22), with industrial contribution from Immuno Cure Holding (HK) Limited. We acknowledge the Nanosystem Fabrication Facility (CWB, HKUST) for assistance with microfabrication; Bioscience Central Research Facility (CWB, HKUST) for providing characterization instrument.

Notes and references

1 M. R. Dunn, R. M. Jimenez and J. C. Chaput, *Nat. Rev. Chem.*, 2017, **1**, 0076.
2 T. Wang, C. Chen, L. M. Larcher, R. A. Barrero and S. Veedu, *Biotechnol. Adv.*, 2019, **37**, 28–50.
3 Y. Zhang, B. S. Lai and M. Juhas, *Molecules*, 2019, **24**, 941.
4 E. Torres-Chavolla and E. C. Alocilja, *Biosens. Bioelectron.*, 2009, **24**, 3175–3182.
5 K. T. Shum, J. Zhou and J. J. Rossi, *Pharmaceuticals*, 2013, **6**, 1507–1542.
6 X. Zhao, X. Dai, S. Zhao, X. Cui, T. Gong, Z. Song, H. Wang and B. Yu, *Spectrochim. Acta, Part A*, 2021, **247**, 119038.
7 Y. M. Chang, M. J. Donovan and W. Tan, *J. Nucleic Acids*, 2013, **2013**, 817350.
8 E. M. McConnell, J. Nguyen and Y. Li, *Front. Chem.*, 2020, **8**, 434.
9 V. T. Nguyen, Y. S. Kwon and M. B. Gu, *Curr. Opin. Biotechnol.*, 2017, **45**, 15–23.

10 Y. Morita, M. Leslie, H. Kameyama, D. E. Volk and T. Tanaka, *Cancers*, 2018, **10**, 80.
11 M. Kim, D. M. Kim, K. S. Kim, W. Jung and D. E. Kim, *Molecules*, 2018, **23**, 830.
12 K. S. Park, *Biosens. Bioelectron.*, 2018, **102**, 179–188.
13 M. Mandal, N. Dutta and G. Dutta, *Anal. Methods*, 2021, **13**, 5400–5417.
14 P. P. Hu, *Inflammation*, 2017, **40**, 295–302.
15 M. Vorobyeva, V. Timoshenko, P. Vorobjev and A. Venyaminova, *Nucleic Acid Ther.*, 2016, **26**, 52–65.
16 G. Zhu, G. Niu and X. Chen, *Bioconjugate Chem.*, 2015, **26**, 2186–2197.
17 Z. Xiao and O. C. Farokhzad, *ACS Nano*, 2012, **6**, 3670–3676.
18 P. Ray and R. R. White, *Pharmaceuticals*, 2010, **3**, 1761–1778.
19 C. Tuerk and L. Gold, *Science*, 1990, **249**, 505–510.
20 A. D. Ellington and J. W. Szostak, *Nature*, 1990, **346**, 818–822.
21 Z. Zhuo, Y. Yu, M. Wang, J. Li, Z. Zhang, J. Liu, X. Wu, A. Lu, G. Zhang and B. Zhang, *Int. J. Mol. Sci.*, 2017, **18**, 2142.
22 R. Stoltenburg, C. Reinemann and B. Strehlitz, *Anal. Bioanal. Chem.*, 2005, **383**, 83–91.
23 J. G. Bruno and J. L. Kiel, *BioTechniques*, 2002, **32**, 178–183.
24 N. Rupcich, R. Nutiu, Y. Li and J. D. Brennan, *Anal. Chem.*, 2005, **77**, 4300–4307.
25 R. K. Mosing, S. D. Mendonsa and M. T. Bowser, *Anal. Chem.*, 2005, **77**, 6107–6112.
26 S. D. Mendonsa and M. T. Bowser, *J. Am. Chem. Soc.*, 2005, **127**, 9382–9383.
27 M. Jing and M. T. Bowser, *Anal. Chem.*, 2013, **85**, 10761–10770.
28 M. Berezovski, M. Musheev, A. Drabovich and S. N. Krylov, *J. Am. Chem. Soc.*, 2006, **128**, 1410–1411.
29 M. V. Berezovski, M. U. Musheev, A. P. Drabovich, J. V. Jitkova and S. N. Krylov, *Nat. Protoc.*, 2006, **1**, 1359–1369.
30 M. Jing and M. T. Bowser, *Lab Chip*, 2011, **11**, 3703–3709.
31 G. Hybarger, J. Bynum, R. F. Williams, J. J. Valdes and J. P. Chambers, *Anal. Bioanal. Chem.*, 2006, **384**, 191–198.
32 C. J. Huang, H. I. Lin, S. C. Shiesh and G. B. Lee, *Biosens. Bioelectron.*, 2010, **25**, 1761–1766.
33 C. J. Huang, H. I. Lin, S. C. Shiesh and G. B. Lee, *Biosens. Bioelectron.*, 2012, **35**, 50–55.
34 H. C. Lai, C. H. Wang, T. M. Liou and G. B. Lee, *Lab Chip*, 2014, **14**, 2002–2013.
35 A. Sinha, P. Gopinathan, Y.-D. Chung, H.-Y. Lin, K.-H. Li, H.-P. Ma, P.-C. Huang, S.-C. Shiesh and G.-B. Lee, *Biosens. Bioelectron.*, 2018, **122**, 104–112.
36 J. Kim, T. R. Olsen, J. Zhu, J. P. Hilton, K.-A. Yang, R. Pei, M. N. Stojanovic and Q. Lin, *Sci. Rep.*, 2016, **6**, 26139.
37 T. R. Olsen, C. Tapia-Alveal, K. Wen, T. S. Worgall, M. N. Stojanovic and Q. Lin, *Biomed. Microdevices*, 2023, **25**, 3.
38 Z. Cao and L. Yobas, *Anal. Chem.*, 2014, **86**, 737–743.
39 Z. Cao and L. Yobas, *ACS Nano*, 2015, **9**, 427–435.
40 L. Duan, Z. Cao and L. Yobas, *Anal. Chem.*, 2017, **89**, 10022–10028.
41 A. Hu, Y. Bu, Y. Liu, Y. C. Lee, S. Ni and L. Yobas, *Lab Chip*, 2025, **25**, 6662–6672.
42 A. Hu, Y. Bu, Y. Liu, Y. C. Lee and L. Yobas, in *2025 IEEE 38th International Conference on Micro Electro Mechanical Systems (MEMS)*, IEEE, 2025, pp. 1221–1224.
43 T. W. Wiegand, P. B. Williams, S. C. Dreskin, M. H. Jouvin, J. P. Kinet and D. Tasset, *J. Immunol.*, 1996, **157**, 221–230.
44 S. D. Mendonsa and M. T. Bowser, *J. Am. Chem. Soc.*, 2004, **126**, 20–21.
45 T. L. Bailey and C. Elkan, *Proc. Int. Conf. Intell. Syst. Mol. Biol.*, 1994, vol. 2, pp. 28–36.
46 M. Zuker, *Nucleic Acids Res.*, 2003, **31**, 3406–3415.
47 S. D. Mendonsa and M. T. Bowser, *Anal. Chem.*, 2004, **76**, 5387–5392.
48 M. Gong, K. R. Wehmeyer, P. A. Limbach and W. R. Heineman, *Electrophoresis*, 2007, **28**, 837–842.
49 R. T. Turgeon, B. R. Fonslow, M. Jing and M. T. Bowser, *Anal. Chem.*, 2010, **82**, 3636–3641.
50 S. Iijima, K. Shiba, Y. Kurihara, S. Kamei, S. Kimura, M. Kimura, H. Kikuchi and I. Kobayashi, *J. Clin. Lab. Anal.*, 1999, **13**, 145–150.
51 X. Ren, M. Bachman, C. Sims, G. P. Li and N. Allbritton, *J. Chromatogr. B: Biomed. Sci. Appl.*, 2001, **762**, 117–125.
52 U. B. Gyllensten and H. A. Erlich, *Proc. Natl. Acad. Sci. U. S. A.*, 1988, **85**, 7652–7656.
53 J. W. Little, I. R. Lehman and A. D. Kaiser, *J. Biol. Chem.*, 1967, **242**, 672–678.
54 T. Hultman, S. Stahl, E. Homes and M. Uhlén, *Nucleic Acids Res.*, 1989, **17**, 4937–4946.
55 A. Nitsche, A. Kurth, A. Dunkhorst, O. Pänke, H. Sielaff, W. Junge, D. Muth, F. Scheller, W. Stöcklein, C. Dahmen, G. Pauli and A. Kage, *BMC Biotechnol.*, 2007, **7**, 48.
56 X. Lou, J. Qian, Y. Xiao, L. Viel, A. E. Gerdon, E. T. Lagally, P. Atzberger, T. M. Tarasow, A. J. Heeger and H. T. Soh, *Proc. Natl. Acad. Sci. U. S. A.*, 2009, **106**, 2989–2994.
57 T. Hünniger, H. Wessels, C. Fischer, A. Paschke-Kratzin and M. Fischer, *Anal. Chem.*, 2014, **86**, 10940–10947.
58 B. Vant-Hull, A. Payano-Baez, R. H. Davis and L. Gold, *J. Mol. Biol.*, 1998, **278**, 579–597.
59 O. Alkhamis, C. Byrd, J. Canoura, A. Bacon, R. Hill and Y. Xiao, *Nucleic Acids Res.*, 2025, **53**, 219.
60 M. Cho, Y. Xiao, J. Nie, R. Stewart, A. T. Csordas, S. S. Oh, J. A. Thomson and H. T. Soh, *Proc. Natl. Acad. Sci. U. S. A.*, 2010, **107**, 15373–15378.
61 J. Yang and M. T. Bowser, *Anal. Chem.*, 2013, **85**, 1525–1530.
62 A. G. Thorsness and A. J. Muscat, *J. Electrochem. Soc.*, 2003, **150**, F219–F228.
63 W. H. Grover, R. H. C. Ivester, E. C. Jensen and R. A. Mathies, *Lab Chip*, 2006, **6**, 623–631.
64 Y. Liu and L. Yobas, *Biomicrofluidics*, 2012, **6**, 046501.
65 J. C. Cox, A. Hayhurst, J. Hesselberth, T. S. Bayer, G. Georgiou and A. D. Ellington, *Nucleic Acids Res.*, 2002, **30**, e108.
66 A. Ozer, J. M. Pagano and J. T. Lis, *Mol. Ther.–Nucleic Acids*, 2014, **3**, e183.
67 M. Darmostuk, S. Rimpelova, H. Gbelcova and T. Ruml, *Biotechnol. Adv.*, 2015, **33**, 1141–1161.

